Deterministic multi-qubit entanglement in a quantum network

Youpeng Zhong,[1, *] Hung-Shen Chang,[1] Audrey Bienfait,[1, †] Étienne Dumur,[1, 2, ‡]
Ming-Han Chou,[1, 3] Christopher R. Conner,[1] Joel Grebel,[1] Rhys G.
Povey,[1, 3] Haoxiong Yan,[1] David I. Schuster,[3, 1] and Andrew N. Cleland[1, 2, §]

[1]*Pritzker School of Molecular Engineering,
University of Chicago, Chicago IL 60637, USA*
[2]*Center for Molecular Engineering and Material Science Division,
Argonne National Laboratory, Argonne IL 60439, USA*
[3]*Department of Physics, University of Chicago, Chicago IL 60637, USA*

Quantum entanglement is a key resource for quantum computation and quantum communication [1]. Scaling to large quantum communication or computation networks further requires the deterministic generation of multi-qubit entanglement [2–4]. The deterministic entanglement of two remote qubits has recently been demonstrated with microwave photons [5–9], optical photons [10] and surface acoustic wave phonons [11]. However, the deterministic generation and transmission of multi-qubit entanglement has not been demonstrated, primarily due to limited state transfer fidelities. Here, we report a quantum network comprising two separate superconducting quantum nodes connected by a 1 meter-long superconducting coaxial cable, where each node includes three interconnected qubits. By directly connecting the coaxial cable to one qubit in each node, we can transfer quantum states between the nodes with a process fidelity of 0.911 ± 0.008. Using the high-fidelity communication link, we can prepare a three-qubit Greenberger-Horne-Zeilinger (GHZ) state [12–14] in one node and deterministically transfer this state to the other node, with a transferred state fidelity of 0.656 ± 0.014. We further use this system to deterministically generate a two-node, six-qubit GHZ state, globally distributed within the network, with a state fidelity of 0.722 ± 0.021. The GHZ state fidelities are clearly above the threshold of $1/2$ for genuine multipartite entanglement [15], and show that this architecture can be used to coherently link together multiple superconducting quantum processors, providing a modular approach for building large-scale quantum computers [16, 17].

Superposition and entanglement are key resources enabling both quantum computing and quantum communication. The deterministic generation and distribution of entanglement in a scalable architecture is thus a central requirement underpinning these technologies. Superconducting qubits show great promise as a scalable approach to building practical quantum computers [18, 19], as well as for coherently linking superconducting processors within a cryostat [5–8] or cryogenically-linked cryostats [20]. Developments in microwave-to-optical transduction promise further extensions of superconducting quantum networks [21, 22], po-

---
* Present Address: Shenzhen Institute for Quantum Science and Engineering, Southern University of Science and Technology, Shenzhen 518055, China

† Present Address: Université de Lyon, ENS de Lyon, Université Claude Bernard, CNRS, Laboratoire de Physique, F-69342 Lyon, France

‡ Present Address: Université Grenoble Alpes, CEA, INAC-Pheliqs, 38000 Grenoble, France

§ Corresponding author; anc@uchicago.edu

tentially allowing for long-distance quantum communication [23, 24]. However, fundamental challenges still remain. In particular, the fidelity of chip-to-chip quantum state transfers, using microwave-frequency photons, has been limited to ~ 0.8 due to losses in the communication channels [5–8, 20], although experiments minimizing this loss point to the potential for high-fidelity communication [9, 25, 26]. Here, we demonstrate a very low-loss connection between two physically-distant quantum nodes fabricated on separate dies, with which we demonstrate a state transfer fidelity of 0.911 ± 0.008. This allows us to deterministically transfer fully-entangled GHZ states between the two nodes, as well as generate a full two-node entangled state, paving the way for modular approaches to large-scale quantum computing and intra-cryostat quantum communication [16].

Our quantum network consists of two nodes A and B, shown in Fig. 1, where each node is a superconducting processor comprising three capacitively-coupled superconducting qubits Q_i^n ($i = 1, 2, 3$; $n = A, B$), with a tunable coupler [27] G^n connected to Q_2^n. We use a 1 m-long niobium-titanium (NbTi) superconducting coaxial cable to connect the two nodes together, with a time-variable coupling strength $g^n(t)$ controlled by the tunable coupler G^n in each node. To build a high-quality communication channel, we avoid use of microwave connectors or circulators [5–8], relying instead on direct superconducting aluminium wirebond connections between the coaxial cable and the processors; see the Supplementary Information [28] for more details.

We place the assembled quantum network in a magnetic shield attached to the mixing chamber of a dilution refrigerator with a base temperature below 10 mK. We first tune up and calibrate the quantum state transfer between Q_2^A and Q_2^B, with the other qubits biased far away in frequency. When the coupling is off, the coaxial cable is effectively shorted to ground on both ends, supporting an evenly-spaced sequence of standing microwave modes, with a free spectral range $\omega_{\text{FSR}}/2\pi = 105$ MHz. The coupling strength g^n between Q_2^n and each mode is determined [28] by the superconducting phase δ^n across the Josephson junction of the coupler G^n. To tune-up each qubit, we isolate the qubits from the cable by biasing the coupler junction to $\delta^n = \pi/2$, turning off the coupling, $g^n \approx 0$. We find each qubit has an intrinsic lifetime of $T_1 \approx 10$ μs and a dephasing time of $T_\phi \approx 3$ μs; see Table S1 [28] for details.

When we prepare the qubit Q_2^A in its excited state $|e\rangle$ and subsequently turn on the coupler G^A to $g^A/2\pi \approx 5.5$ MHz, we observe a sequence of vacuum Rabi oscillations between
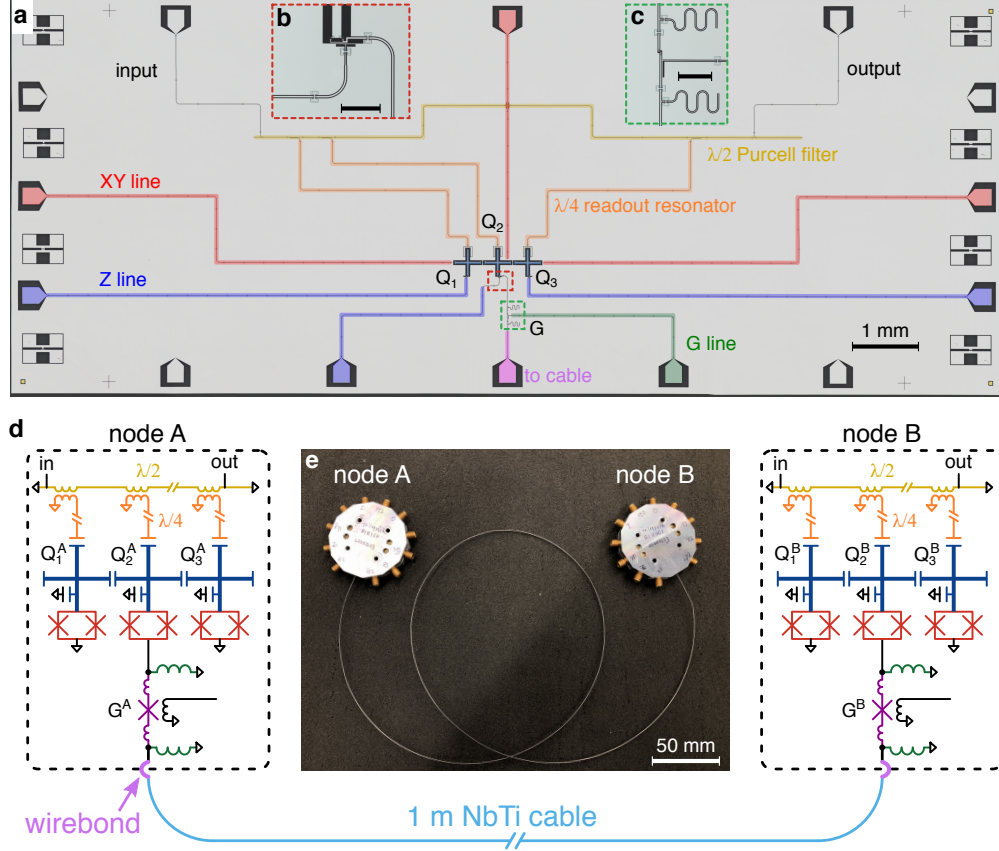
Figure 1. **Device description. a,** False-color micrograph of one quantum processor node, consisting of three capacitively-coupled superconducting qubits Q_i $(i = 1, 2, 3)$ with a tunable coupler G connected to Q_2. **b, c,** Higher-magnification micrographs of the Q_2 Josephson junctions and the tunable coupler G, respectively. Scale bars are 100 μm. **d,** Schematic of the quantum network, consisting of two nodes A and B connected by a 1 m-long superconducting NbTi coaxial cable. Each node is a quantum processor of the type shown in panel **a**. **e,** Photograph of the quantum network assembly, where each node is in a machined aluminium sample holder connected internally to the superconducting cable.

Q_2^A and the cable standing modes as we vary the qubit frequency and the interaction time, shown in Fig. 2a. As the mode at 5.798 GHz (dashed line) has a slightly longer lifetime $(T_{1r} = 473$ ns) than the other modes, we use this as the communication mode R. The on-resonant vacuum Rabi oscillation between Q_2^A and R is shown in detail in Fig. 2b; more details are provided in the Supplementary Information [28].

If both qubits Q_2^A and Q_2^B are resonantly-coupled to R, the tripartite system has a

4

"dark" and two "bright" eigenmodes, with very little occupation of the cable in the dark eigenmode [25]. As proposed in Ref. 29 and demonstrated in Refs. 8 and 25, high-fidelity quantum state transfers can be achieved using the dark eigenmode even in the presence of significant cable loss, albeit with limited transfer rates. As we have both cable and qubit loss, we implement a hybrid state transfer scheme [29], which involves all three eigenmodes in a way that balances these different losses. The hybrid scheme involves setting both G^A and G^B to the same coupling strength $g_0/2\pi = 4$ MHz while tuning both Q_2^A and Q_2^B to be resonant with R for a duration τ, shown in Fig. 2c. At $\tau = 72$ ns, one photon is transferred from node A to node B with an efficiency $\eta = 0.881 \pm 0.008$; numerical simulations including the measured loss are in excellent agreement with the measurements [28]. We perform quantum process tomography to characterize this state transfer (ST) process, yielding the process matrix χ shown in Fig. 2d, with a process fidelity $\mathcal{F}^p = \text{Tr}(\chi \cdot \chi_{\text{ideal}}) = 0.911 \pm 0.008$, where χ_{ideal} is the process matrix for the identity operation $\mathcal{I}$. Numerical simulations give a process fidelity of 0.920. These simulations imply that the ST process could be further improved by reducing loss associated with the cable and its interconnects [28].

In addition to the single-qubit state transfer process, we tune up controlled-NOT (CNOT) gates built from controlled-Z (CZ) gates combined with single-qubit $\pi/2$ rotations, as well as tuning up iSWAP gates. The iSWAP gate is implemented by biasing Q_j^n ($j = 1, 3$) to be resonant with Q_2^n for a duration $\tau_{\text{swap}} = \pi/2g_{j,2}^n \approx 15$ ns, where $g_{j,2}^n/2\pi \approx 16.7$ MHz is the capacitive coupling strength between Q_j^n and Q_2^n. The CZ gate is implemented [30] by biasing Q_j^n to be resonant with the $|e\rangle$-$|f\rangle$ transition frequency of Q_2^n for a duration $\tau_{\text{CZ}} = \pi/\sqrt{2}g_{j,2}^n \approx 21$ ns, completing an $|ee\rangle \to -i|gf\rangle \to -|ee\rangle$ process that acquires an overall phase of π for the $|ee\rangle$ state, leaving the other basis states unchanged. We characterize [28] the CZ gate using quantum process tomography, obtaining a process matrix χ_{CZ} with an average process fidelity of 0.950 ± 0.006.

We use these gates to deterministically generate a GHZ state [12–14] in node A, $|\psi_{\text{GHZ}}\rangle = (|ggg\rangle + |eee\rangle)\sqrt{2}$ (written as $|Q_1^A Q_2^A Q_3^A\rangle$), which we then transfer to node B, using the protocol shown in Fig. 3a. This involves two CNOT gates to prepare the state followed by three sequential transfers (ST) through the cable using Q_2^n ($n = A, B$), interleaved with iSWAPs with Q_1^n or Q_3^n.

The density matrix ρ^A of the three-qubit GHZ state in node A is measured using quantum state tomography and shown in Fig. 3b, with a state fidelity $\mathcal{F}^A = \langle\psi_{\text{GHZ}}|\rho^A|\psi_{\text{GHZ}}\rangle =$

0.931 ± 0.012. Calculations using χ_{CZ} give a state fidelity of 0.938, in good agreement with the experiment. This state is then transferred to node B using three sequential transfers with interleaved iSWAP gates, yielding the final state ρ^B in node B, as shown in Fig. 3c, with a GHZ state fidelity $\mathcal{F}^B = 0.656 \pm 0.014$, clearly above the threshold of $1/2$ for genuine multipartite entanglement [15]. A calculation applying $\chi^{\otimes 3}$ and the expected decoherence process to ρ^A gives a state fidelity of 0.648, agreeing well with experiment.

Finally, we demonstrate the step-by-step generation of a six-qubit entangled state distributed in the network, using the protocol shown in Fig. 4a. In step I, we prepare a Bell triplet state $|B+\rangle = (|gg\rangle + |ee\rangle)/\sqrt{2}$ (written as $|Q_2^A Q_2^B\rangle$), using an ST/2 process similar to the ST process, except the qubit frequencies and coupling parameters are adjusted [28] so that an optimal Bell state fidelity is achieved at $\tau = 62.8$ ns. The density matrix ρ_I for this process is shown in Fig. 4b, with a state fidelity of 0.908 ± 0.012. Numerical simulations [28] yield a state fidelity of 0.915. In step II, we apply CNOT gates between Q_1^n and Q_2^n to transform the Bell state into a four-qubit GHZ state $(|gggg\rangle + |eeee\rangle)/\sqrt{2}$ (written as $|Q_1^A Q_2^A Q_1^B Q_2^B\rangle$), with a density matrix ρ_{II} displayed in Fig. 4c with state fidelity 0.814 ± 0.008. We finally apply CNOT gates between Q_2^n and Q_3^n, creating a six-qubit GHZ state $(|gggggg\rangle + |eeeeee\rangle)/\sqrt{2}$ (written as $|Q_1^A Q_2^A Q_3^A Q_1^B Q_2^B Q_3^B\rangle$). The density matrix ρ_{III} of the entangled state is shown in Fig. 4d, with a state fidelity of 0.722 ± 0.021, clearly above the threshold of $1/2$ for genuine multipartite entanglement [15]. Numerical calculations [28] give ρ_{II} and ρ_{III} with state fidelities of 0.829 and 0.738 respectively, agreeing well with the experiment.

In conclusion, we have built a two-node quantum network consisting of two three-qubit superconducting processor nodes connected by a 1 m-long superconducting coaxial cable. Using this system, we achieve a state transfer process fidelity of 0.911 ± 0.008 between the two nodes, which supports the deterministic generation and transfer of multi-qubit GHZ states. The transfer fidelity here is primarily limited by loss in the cable connections; improving these connections should yield significant increases in the channel coherence and transfer fidelities. This architecture can be extended to coherently link more than two processor nodes, providing a modular solution for building large-scale quantum computers [16, 17].
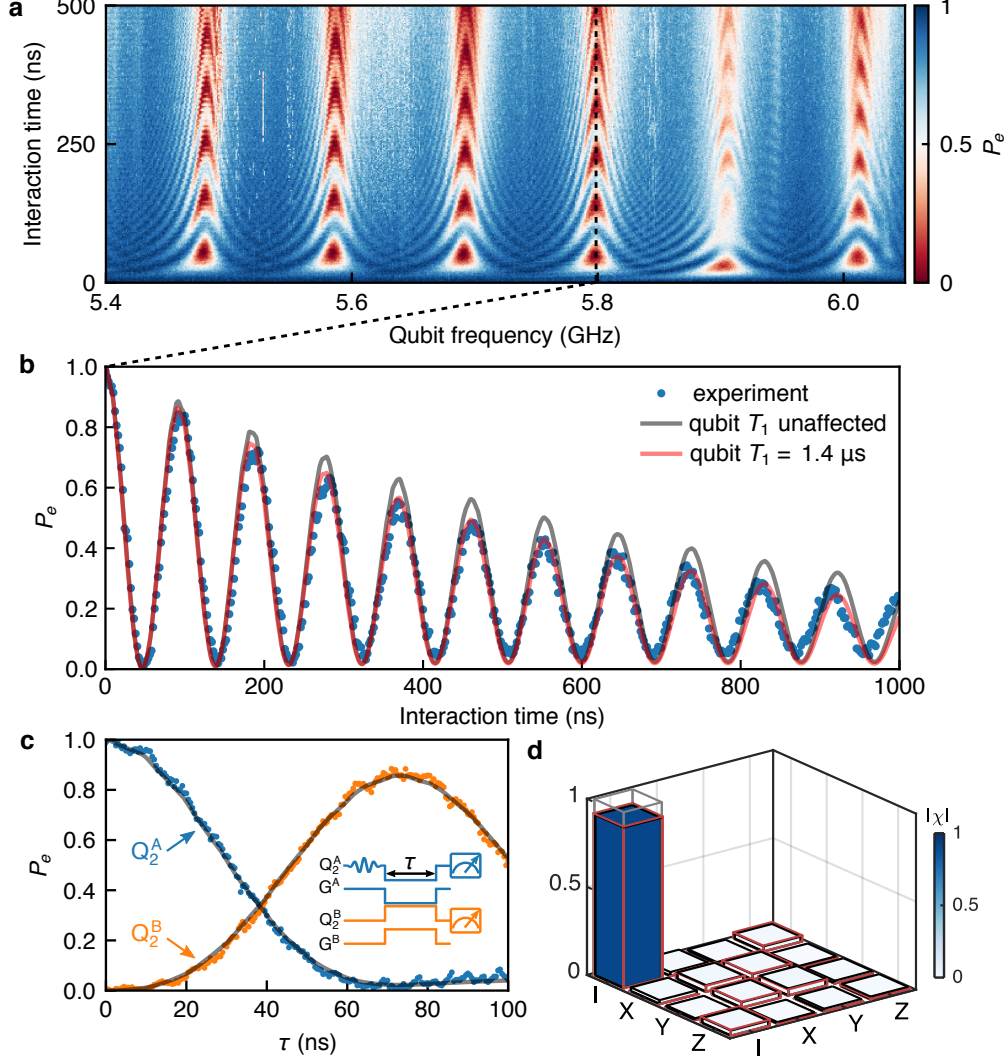
Figure 2. **Quantum state transfer between node A and node B. a,** Vacuum Rabi oscillations between Q_2^A and six standing modes in the coaxial cable, with the coupling strength $g^A/2\pi \approx 5.5$ MHz. **b,** Slice through data in **a**, showing the vacuum Rabi oscillation of Q_2^A with the communication mode R at 5.798 GHz. Numerical simulations suggest the effective qubit T_1 is shortened to 1.4 μs during the interaction, due to loss associated with the cable connections [28]. **c,** Quantum state transfer from node A to node B using a hybrid transfer scheme, where Q_2^A and Q_2^B are resonantly coupled to R with the same coupling strength $g_0/2\pi = 4$ MHz for a duration τ. At $\tau = 72$ ns, we achieve a single photon transfer efficiency of $\eta = 0.881 \pm 0.008$. Grey lines: Numerical simulations. Inset: Control pulse sequence. **d,** Process matrix χ for the quantum state transfer, corresponding to a process fidelity $\mathcal{F}^p = 0.911 \pm 0.008$. The solid bars and red and grey frames are the measured, simulated and ideal values respectively.
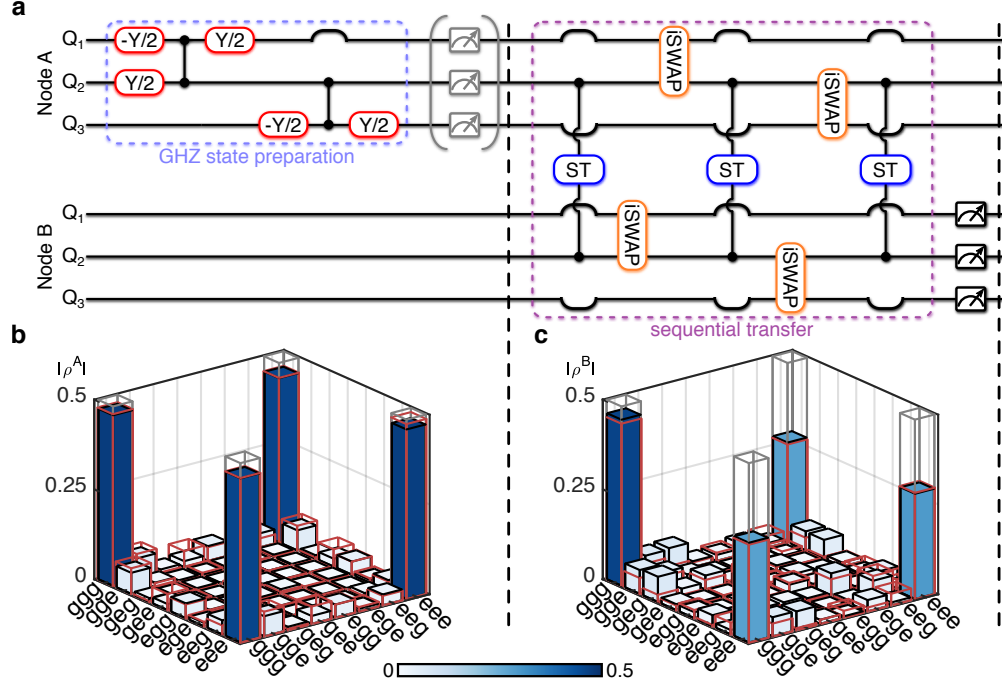
Figure 3. **Deterministic transfer of a three-qubit GHZ state. a,** Schematic of the GHZ state preparation and the sequential transfer protocol. Bumps in the horizontal lines are detuning pulses applied to Q_j^n $(j = 1, 3)$ to minimize interactions between these qubits and Q_2^n during the ST and CZ operations. Measurement of the qubits in node A is only done to characterize the prepared GHZ state, and is not performed when transferring the state to node B. **b,** Density matrix ρ^A of the GHZ state prepared in node A, with a state fidelity of 0.931 ± 0.012. **c,** Density matrix ρ^B of the state received in node B, with a state fidelity of 0.656 ± 0.014. Solid bars and red and grey frames are measured, simulated, and ideal values, respectively.
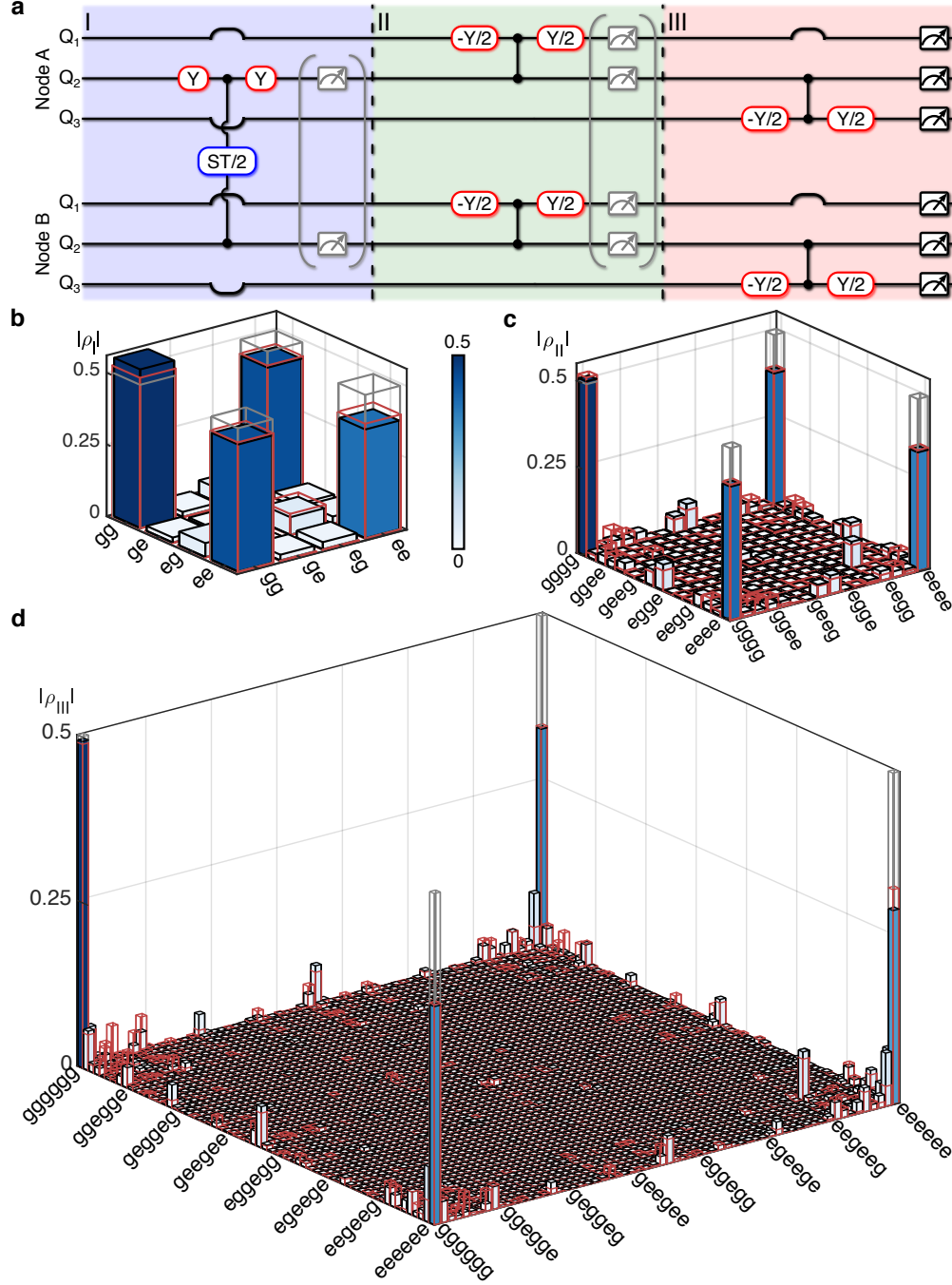
Figure 4. **Deterministic generation of multi-qubit entanglement in a quantum network.**
a, The step-by-step protocol for entangling the two nodes A and B. Here the ST/2 process involves transmitting half a photon from Q_2^A to Q_2^B. Bumps in the horizontal lines are detuning pulses. **b,** The Bell triplet state between Q_2^A and Q_2^B created in step I, with a state fidelity of 0.908 ± 0.012. **c,** The four-qubit GHZ state created in step II, with a state fidelity of 0.814 ± 0.008. **d,** The six-qubit GHZ state created in step III, with a state fidelity of 0.722 ± 0.021. The solid bars and red and grey frames are the measured, simulated and ideal values respectively.

9

[1] Nielsen, M. A. & Chuang, I. L. *Quantum computation and quantum information* (Cambridge University Press, 2010), 2 edn.

[2] Gottesman, D. & Chuang, I. L. Demonstrating the viability of universal quantum computation using teleportation and single-qubit operations. *Nature* **402**, 390–393 (1999).

[3] Duan, L.-M., Lukin, M. D., Cirac, J. I. & Zoller, P. Long-distance quantum communication with atomic ensembles and linear optics. *Nature* **414**, 413–418 (2001).

[4] Jiang, L., Taylor, J. M., Sørensen, A. S. & Lukin, M. D. Distributed quantum computation based on small quantum registers. *Physical Review A* **76**, 062323 (2007).

[5] Kurpiers, P. *et al.* Deterministic quantum state transfer and remote entanglement using microwave photons. *Nature* **558**, 264–267 (2018).

[6] Axline, C. J. *et al.* On-demand quantum state transfer and entanglement between remote microwave cavity memories. *Nature Physics* **14**, 705–710 (2018).

[7] Campagne-Ibarcq, P. *et al.* Deterministic remote entanglement of superconducting circuits through microwave two-photon transitions. *Physical Review Letters* **120**, 200501 (2018).

[8] Leung, N. *et al.* Deterministic bidirectional communication and remote entanglement generation between superconducting qubits. *npj Quantum Information* **5**, 18 (2019).

[9] Zhong, Y. P. *et al.* Violating Bell's inequality with remotely connected superconducting qubits. *Nature Physics* **15**, 741–744 (2019).

[10] Humphreys, P. C. *et al.* Deterministic delivery of remote entanglement on a quantum network. *Nature* **558**, 268–273 (2018).

[11] Bienfait, A. *et al.* Phonon-mediated quantum state transfer and remote qubit entanglement. *Science* **364**, 368–371 (2019).

[12] Greenberger, D. M., Horne, M. A., Shimony, A. & Zeilinger, A. Bell's theorem without inequalities. *American Journal of Physics* **58**, 1131–1143 (1990).

[13] Neeley, M. *et al.* Generation of three-qubit entangled states using superconducting phase qubits. *Nature* **467**, 570–573 (2010).

[14] DiCarlo, L. *et al.* Preparation and measurement of three-qubit entanglement in a superconducting circuit. *Nature* **467**, 574–578 (2010).

[15] Gühne, O. & Seevinck, M. Separability criteria for genuine multiparticle entanglement. *New*

Journal of Physics **12**, 053002 (2010).

[16] Monroe, C. *et al.* Large-scale modular quantum-computer architecture with atomic memory and photonic interconnects. *Physical Review A* **89**, 022317 (2014).

[17] Chou, K. S. *et al.* Deterministic teleportation of a quantum gate between two logical qubits. *Nature* **561**, 368–373 (2018).

[18] Arute, F. *et al.* Quantum supremacy using a programmable superconducting processor. *Nature* **574**, 505–510 (2019).

[19] Rosenberg, D. *et al.* Solid-state qubits: 3D integration and packaging. *IEEE Microwave Magazine* **21**, 72–85 (2020).

[20] Magnard, P. *et al.* Microwave quantum link between superconducting circuits housed in spatially separated cryogenic systems. *arXiv preprint arXiv:2008.01642* (2020).

[21] Bochmann, J., Vainsencher, A., Awschalom, D. D. & Cleland, A. N. Nanomechanical coupling between microwave and optical photons. *Nature Physics* **9**, 712–716 (2013).

[22] Mirhosseini, M., Sipahigil, A., Kalaee, M. & Painter, O. Quantum transduction of optical photons from a superconducting qubit. *arXiv preprint arXiv:2004.04838* (2020).

[23] Hensen, B. *et al.* Loophole-free Bell inequality violation using electron spins separated by 1.3 kilometres. *Nature* **526**, 682–686 (2015).

[24] Liao, S.-K. *et al.* Satellite-to-ground quantum key distribution. *Nature* **549**, 43–47 (2017).

[25] Chang, H.-S. *et al.* Remote entanglement via adiabatic passage using a tunably-dissipative quantum communication system. *Physical Review Letters* **124**, 240502 (2020).

[26] Burkhart, L. D. *et al.* Error-detected state transfer and entanglement in a superconducting quantum network. *arXiv preprint arXiv:2004.06168* (2020).

[27] Chen, Y. *et al.* Qubit architecture with high coherence and fast tunable coupling. *Physical Review Letters* **113**, 220502 (2014).

[28] Zhong, Y. *et al.* Supplementary Information for "Deterministic multi-qubit entanglement in a quantum network" (2020).

[29] Wang, Y.-D. & Clerk, A. A. Using dark modes for high-fidelity optomechanical quantum state transfer. *New Journal of Physics* **14**, 105010 (2012).

[30] Strauch, F. W. *et al.* Quantum logic gates for coupled superconducting phase qubits. *Physical Review Letters* **91**, 167005 (2003).

[31] Julsgaard, B., Kozhekin, A. & Polzik, E. S. Experimental long-lived entanglement of two

macroscopic objects. *Nature* **413**, 400–403 (2001).

[32] Chou, C.-W. *et al.* Measurement-induced entanglement for excitation stored in remote atomic ensembles. *Nature* **438**, 828–832 (2005).

[33] Moehring, D. L. *et al.* Entanglement of single-atom quantum bits at a distance. *Nature* **449**, 68–71 (2007).

[34] Ritter, S. *et al.* An elementary quantum network of single atoms in optical cavities. *Nature* **484**, 195–200 (2012).

[35] Lee, K. C. *et al.* Entangling macroscopic diamonds at room temperature. *Science* **334**, 1253–1256 (2011).

[36] Bernien, H. *et al.* Heralded entanglement between solid-state qubits separated by three metres. *Nature* **497**, 86–90 (2013).

[37] Roch, N. *et al.* Observation of measurement-induced entanglement and quantum trajectories of remote superconducting qubits. *Physical Review Letters* **112**, 170501 (2014).

[38] Narla, A. *et al.* Robust concurrent remote entanglement between two superconducting qubits. *Physical Review X* **6**, 031036 (2016).

[39] Dickel, C. *et al.* Chip-to-chip entanglement of transmon qubits using engineered measurement fields. *Physical Review B* **97**, 064508 (2018).

[40] Kurpiers, P. *et al.* Quantum communication with time-bin encoded microwave photons. *Physical Review Applied* **12**, 044067 (2019).

[41] Sillanpää, M. A., Park, J. I. & Simmonds, R. W. Coherent quantum state storage and transfer between two phase qubits via a resonant cavity. *Nature* **449**, 438–442 (2007).

[42] Majer, J. *et al.* Coupling superconducting qubits via a cavity bus. *Nature* **449**, 443–447 (2007).

[43] Baksic, A., Ribeiro, H. & Clerk, A. A. Speeding up adiabatic quantum state transfer by using dressed states. *Physical Review Letters* **116**, 230503 (2016).

[44] Zhou, B. B. *et al.* Accelerated quantum control using superadiabatic dynamics in a solid-state lambda system. *Nature Physics* **13**, 330–334 (2017).

[45] Cirac, J. I., Zoller, P., Kimble, H. J., & Mabuchi, H. Quantum state transfer and entanglement distribution among distant nodes in a quantum network. *Physical Review Letters* **78**, 3221–3224 (1997).

[46] Korotkov, A. N. Flying microwave qubits with nearly perfect transfer efficiency. *Physical*

Review B **84**, 014510 (2011).

[47] Sete, E. A., Mlinar, E. & Korotkov, A. N. Robust quantum state transfer using tunable couplers. *Physical Review B* **91**, 144509 (2015).

[48] Yin, Y. *et al.* Catch and release of microwave photon states. *Physical Review Letters* **110**, 107001 (2013).

[49] Wenner, J. *et al.* Catching time-reversed microwave coherent state photons with 99.4% absorption efficiency. *Physical Review Letters* **112**, 210501 (2014).

[50] Srinivasan, S. J. *et al.* Time-reversal symmetrization of spontaneous emission for quantum state transfer. *Physical Review A* **89**, 033857 (2014).

[51] Pechal, M. *et al.* Microwave-controlled generation of shaped single photons in circuit quantum electrodynamics. *Physical Review X* **4**, 041010 (2014).

[52] Zeytinoğlu, S. *et al.* Microwave-induced amplitude-and phase-tunable qubit-resonator coupling in circuit quantum electrodynamics. *Physical Review A* **91**, 043846 (2015).

[53] Xiang, Z. L., Zhang, M., Jiang, L. & Rabl, P. Intracity quantum communication via thermal microwave networks. *Physical Review X* **7**, 011035 (2017).

[54] Vermersch, B., Guimond, P.-O., Pichler, H. & Zoller, P. Quantum state transfer via noisy photonic and phononic waveguides. *Physical Review Letters* **118**, 133601 (2017).

[55] Steffen, M. *et al.* Measurement of the entanglement of two superconducting qubits via state tomography. *Science* **313**, 1423–1425 (2006).

[56] Neeley, M. *et al.* Process tomography of quantum memory in a Josephson-phase qubit coupled to a two-level state. *Nature Physics* **4**, 523–526 (2008).

Acknowledgements

Author contributions

Y.P.Z. designed and fabricated the devices, performed the measurement and analyzed the data. H.-S.C. provided help with the measurement. A.B. and É.D. provided help with the infrastructure setup. A.N.C. and D.I.S. advised on all efforts. All authors contributed to discussions and production of the manuscript.

Competing interests

The authors declare no competing interests.

Methods

Quantum state transfer and remote entanglement protocols. Probabilistic remote entanglement has been realized with atomic ensembles [31, 32], single atoms [33, 34], defects in diamond [23, 35, 36] and superconducting qubits [37–40]. However these probabilistic approaches are not scalable; a deterministic approach is preferable for large-scale quantum networks. For short-distance communication, for example with microwave cables shorter than a few meters, the free spectral range of the cable is large enough that a single standing mode can relay quantum states [9, 41, 42], or state transfers can be via a "dark"

mode hybridized by a standing mode and the on-chip elements (qubits or resonators) [8, 25]. Here, we use a hybrid scheme [29] for state transfer, which balances the loss in the channel with that in the qubits, which might be further improved by optimizing the transfer process using shortcut-to-adiabatic-passage protocols [43, 44].

If the length of the cable is increased, the free spectral range of the standing modes in the cable becomes smaller, making single-mode quantum state transfers more challenging. For long-distance communication, the use of itinerant photons is preferable [45–47] but challenging in practice. Using tunable couplers to shape the photon emission and capture in a time-reversal symmetric manner, high-fidelity quantum state transfers have been achieved with itinerant photons [5–7, 48–52]; proposals using a chiral communication channels point to the potential for quantum state transfers over thermal microwave networks [53, 54]. As demonstrated in earlier work [9], the communication architecture here can also use itinerant photons to perform high-fidelity quantum state transfers.

Quantum state and process tomography. The density matrices of the Bell state and the GHZ states are characterised using quantum state tomography [55]. After the state preparation and transfer, gates from the set $\{I, X/2, Y/2\}$ are applied to each qubit before the simultaneous readout of all qubits; the measured probabilities are corrected for readout errors, and the density matrix is reconstructed numerically. We use CVX, a Matlab package for specifying and solving convex programs, to reconstruct the density matrix while constraining it to be Hermitian, to have unit trace, and to be positive semidefinite. The single-shot simultaneous readout of the qubits is repeated 3×10^3 times to obtain the measured probabilities; the state tomography is run repeatedly, in each repeat we reconstruct the density matrix and obtain the state fidelity. The fidelities and uncertainties of the quantum states correspond to the mean and standard deviation of 100 repeated measurements.

Quantum process tomography [56] for the state transfer is carried out by preparing Q_2^A in the input states $\{|g\rangle, (|g\rangle - i|e\rangle)/\sqrt{2}, (|g\rangle + |e\rangle)/\sqrt{2}, |e\rangle\}$, then performing the quantum state transfer process. The corresponding outcome density matrix in Q_2^B is measured using quantum state tomography as described above. The process matrix is reconstructed using the input and outcome density matrices, using the CVX package to constrain it to be Hermitian, unit trace, and positive semidefinite.

Data availability

The data that support the plots within this paper and other findings of this study are available from the corresponding author upon reasonable request.

Supplementary Information for "Deterministic multi-qubit entanglement in a quantum network"

Youpeng Zhong,[1, *] Hung-Shen Chang,[1] Audrey Bienfait,[1, †] Étienne Dumur,[1, 2, ‡]

Ming-Han Chou,[1, 3] Christopher R. Conner,[1] Joel Grebel,[1] Rhys G.

Povey,[1, 3] Haoxiong Yan,[1] David I. Schuster,[3, 1] and Andrew N. Cleland[1, 2, §]

[1]*Pritzker School of Molecular Engineering,*

University of Chicago, Chicago IL 60637, USA

[2]*Center for Molecular Engineering and Material Science Division,*

Argonne National Laboratory, Argonne IL 60439, USA

[3]*Department of Physics, University of Chicago, Chicago IL 60637, USA*

I. DEVICE FABRICATION

The device fabrication recipe is adapted from Refs. 1–3, with some modifications to simplify the fabrication of the air-bridge crossovers.

Fabrication steps preceding definition of the qubit and coupler Josephson junctions are done on a 100 mm-diameter sapphire wafer. The wafer is then cut into four quarters, allowing for more attempts for the more delicate junction fabrication.

1. 100 nm Al base layer deposition using electron beam evaporation.

2. Base layer photolithography and dry etch with $BCl_3/Cl_2/Ar$ inductively coupled plasma (ICP). This defines the qubit capacitors, the tunable coupler wiring, and the readout and control circuitry.

3. 200 nm crossover scaffold SiO_2 deposition using photolithography, electron beam evaporation and liftoff.

4. 10 nm/150 nm Ti/Au alignment mark layer deposition using photolithography, electron beam evaporation and liftoff.

5. Josephson junction deposition using the Dolan bridge method [4] using shadow evaporation and liftoff, using a PMMA/MAA bilayer and electron beam lithography. The Al evaporated in this step does not have any galvanic contact with the base layer wiring.

6. 300 nm crossover and bandage layer: Al liftoff deposition, preceded by an *in situ* Ar ion mill. This step [5] creates the top Al layer for crossovers, as well as establishes galvanic connections between the base wiring Al from step 1 and the Josephson junctions defined in step 5.

7. Vapor HF etch to remove the SiO_2 scaffold underlying the Al crossovers from step 3.

* Present Address: Shenzhen Institute for Quantum Science and Engineering, Southern University of Science and Technology, Shenzhen 518055, China

† Present Address: Université de Lyon, ENS de Lyon, Université Claude Bernard, CNRS, Laboratoire de Physique, F-69342 Lyon, France

‡ Present Address: Université Grenoble Alpes, CEA, INAC-Pheliqs, 38000 Grenoble, France

§ Corresponding author; anc@uchicago.edu

We use 0.9 μm I-line photoresist AZ MiR 703 for all photolithography steps. The base layer lithography (step 2) uses AZ 300 MIF developer. The other steps (step 3, 4 and 6) use AZ 1:1 developer, which does not attack aluminum. Because the SiO$_2$ scaffold layer (step 3) and the crossover layer (step 6) here involve much thinner deposited layers than those in Refs. 1 and 3, a thick layer of AZ 703 photoresist is sufficient for the lift-off process, which greatly simplifies the fabrication recipe, as compared to the use of tri-layer positive photoresist in Ref. 3 or negative photoresist in Ref. 1. Furthermore, the crossover layer is now merged with the bandage layer [5] (step 6) here, further simplifying the fabrication process. Note the air-bridge is mechanically fragile and cannot sustain sonication.
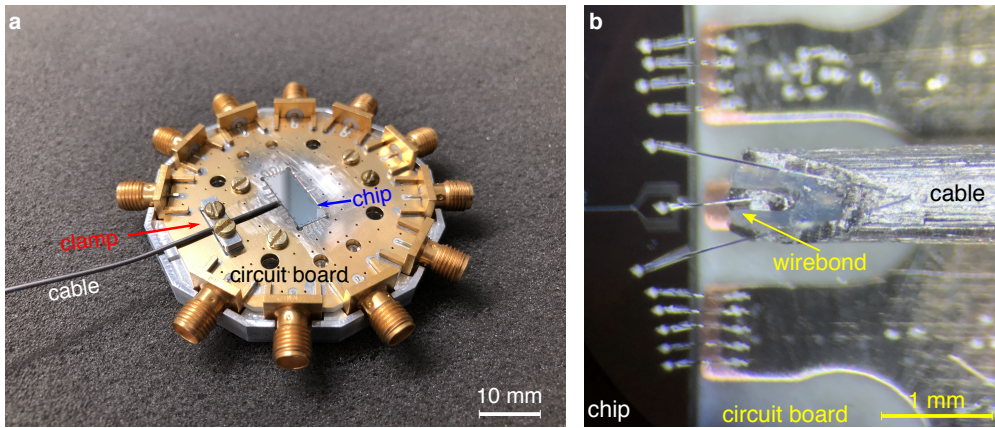
II. CABLE-CHIP WIREBOND CONNECTIONS

Figure S1. Cable-chip wirebond connection. **a,** Image of the sample holder consisting of a gold-plated printed circuit board, non-magnetic SMA connectors and an aluminum enclosure (the top part of which is removed here). The NbTi cable is held close to the chip, then firmly clamped to the sample holder. **b,** Image showing the wirebond connection between the coaxial cable and the processor chip.

In this experiment, we use a 1 meter long niobium-titanium (NbTi) superconducting coaxial cable (manufacturer: COAX CO., LTD., part number: SC-086/50-NbTi-NbTi) to connect the two superconducting quantum processors. To achieve a high-quality communication channel connection, we avoid the use of normal-metal connectors (e.g. SMA connectors) and instead use 25 μm diameter aluminum wirebonds to connect the cable directly to the superconducting processor chip. A sample holder specifically designed for this purpose is

3

used here, as shown in Fig. S1a. The NbTi coaxial cable is held close to the processor chip and then firmly clamped on the sample holder with a clamp. The top part of the outer conductor and the PTFE dielectric is removed with a sharp blade to expose the inner conductor at the end of the cable, as shown in Fig. S1b. The top surfaces of the inner and outer conductors are carefully scraped with a sharp blade to create a flat surface for wirebonding.

The quality factor of the communication channel varies in different assembled devices, depending strongly on the quality of the wirebond connection. To further explore the loss mechanism in the communication channel, we performed a separate cable test experiment, where we directly wirebond the NbTi cable to a short coplanar waveguide (CPW) line of length $\ell_c \approx 3$ mm on a test chip, see Fig. S2. A network analyzer measurement is carried out [6], yielding the quality factor Q of each standing mode (blue dots). We observe a clear trend of Q increasing with frequency in this cable test. For comparison, we also plot the Q of the standing modes measured in the experiment in the main text (orange dots), and see a similar trend, except some modes have a significantly lower Q, likely due to spurious two-level state (TLS) defects near the resonant frequency. The overall frequency dependence is consistent with a resistive dissipation channel R_s in the wirebond interface, as shown inset in Fig. S2. This could originate from a thick oxide barrier layer on the NbTi surface. For simplicity, we assume the current of a standing cable mode follows a simple cosine shape along the CPW line. In the wirebond interface, the current is $I_0 \cos(\beta_c \ell_c)$ where I_0 is the current amplitude at the shorted end, and β_c is the propagation constant for the CPW line. This current gives a power loss $P_{\text{loss}} = I_0^2 \cos^2(\beta_c \ell_c) R_s$, corresponding to a quality factor of [7]

$$Q_{\text{loss}} = \omega_m \frac{L_m I_0^2}{P_{\text{loss}}} = \omega_m \frac{L_m}{\cos^2(\beta_c \ell_c) R_s}, \tag{S1}$$

where $\omega_m / 2\pi$ is the standing mode frequency and L_m the lumped element inductance of the mode (see section V). The Q of the standing mode is then given by

$$1/Q = 1/Q_{\text{loss}} + 1/Q_0, \tag{S2}$$

where Q_0 is the cable's intrinsic quality factor. Fitting this model with the cable test data, we obtain $R_s = 0.38$ Ω and $Q_0 = 90.9 \times 10^3$, shown by the grey line in Fig. S2.

In Ref. 8, Kurpiers *et al.* reported an intrinsic Q as high as 92×10^3 for a NbTi coaxial cable made by Keycom Corp., using capacitive coupling. In Ref. 9, a NbTi cable of the same kind used in this experiment is capacitively-coupled to a 3D transmon qubit, where typical

Q's of order 50×10^3 with occasional values as high as 160×10^3 were observed. The cable intrinsic Q values are quite similar, likely limited by the dielectric loss of PTFE at cryogenic temperatures.

According to the model in Fig. S2, if we adjust the coupler circuit such that $\ell_c \sim \lambda/4$, where λ is the wavelength of the chip standing mode, then $\cos(\beta_c \ell_c) \approx 0$, minimizing the loss through R_s for frequencies close to the resonant frequency of the $\lambda/4$ transformer. Alternatively, if we use a capacitive tunable coupler design [10], then the channel is open on both ends, and the loss through R_s will be small, as long as $\ell_c \ll \lambda/4$. Another approach is to minimize R_s by using an Al cable instead of NbTi, although cables clad in Al are not easily available.
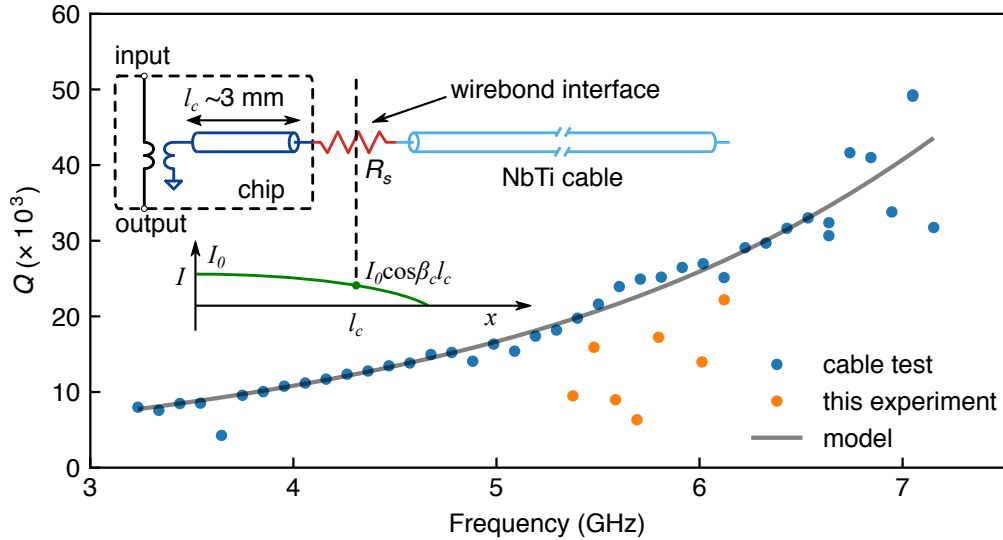

Figure S2. Channel loss from the wirebond connection. Inset: Schematic of independent measurement of coaxial cable loss, where the cable is wirebonded to a short CPW line of length $\ell_c \sim 3$ mm on a test chip. The loss in the wirebond interface is modeled as a series resistance R_s. The current distribution of a standing mode is assumed to follow a simple cosine shape along the CPW line, ignoring the transition in the wirebond interface. Blue dots represent the Q of each standing mode measured in this experiment; orange dots are from experiments in main text. Grey line is numerical model with $R_s = 0.38\ \Omega$ and $Q_0 = 90.9 \times 10^3$.
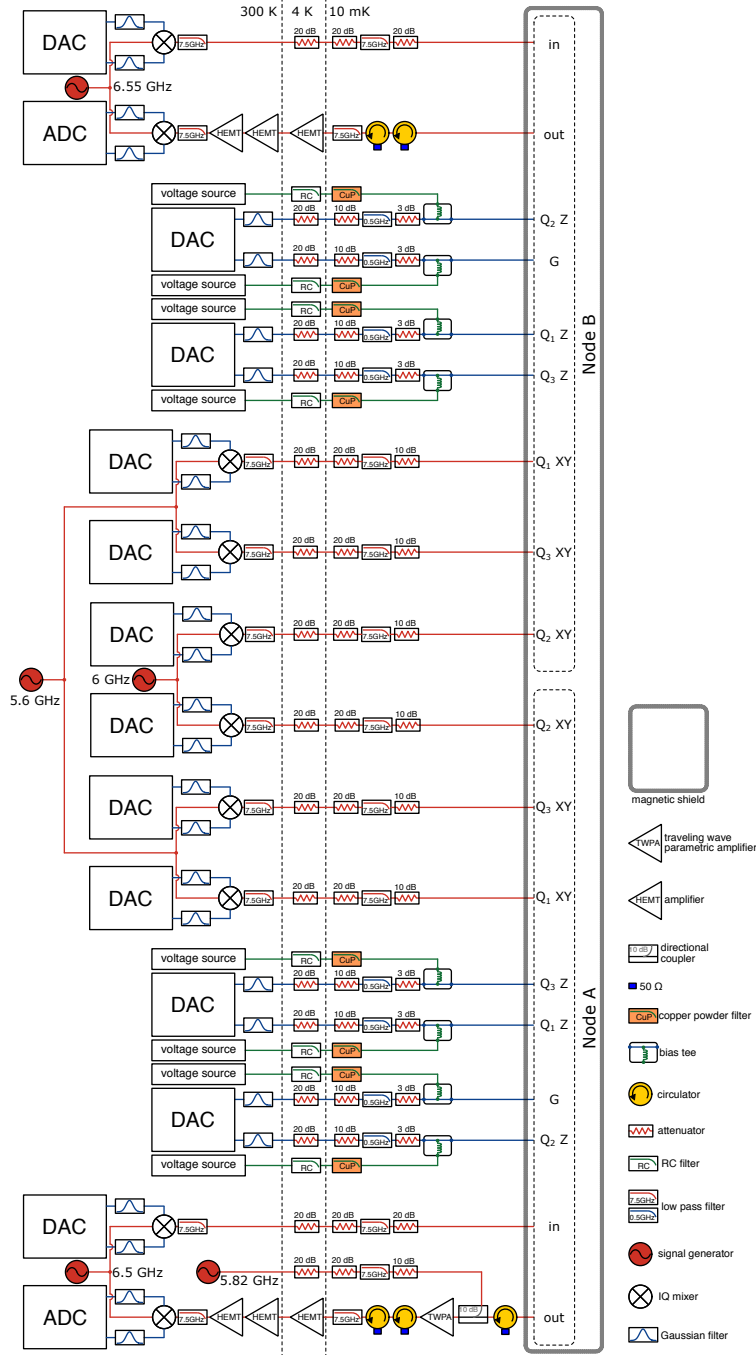
III. EXPERIMENTAL SETUP

Figure S3. Schematic of the experimental setup.

A schematic of the room-temperature electronics and the cryogenic wiring is shown in Fig. S3, similar to that in Ref. 1. We use custom digital-to-analog converter (DAC) (dual-channel, 14-bit resolution, 1 GS/s sampling rate) and analog-to-digital converter (ADC)

(dual-channel, 8-bit resolution, 1 GS/s sampling rate) circuit boards for qubit control and measurement, respectively. Each control signal output and measurement signal input channel is filtered by a custom Gaussian low-pass filter with a -3 dB bandwidth of about 250 MHz.

The DAC boards can generate nanosecond-length pulses for fast qubit Z or coupler G control. The fast bias pulse is combined with a direct-current (DC) bias using a bias-tee at the 10 mK stage, where the DC bias line is filtered with an RC filter of ~ 1 MHz bandwidth at the 4 K stage and a copper powder filter at the 10 mK stage. The DAC dual-channel output can also modulate the envelope of an IQ mixer for qubit XY rotations, or to drive the readout resonator for dispersive measurements. The modulation of the IQ mixer can provide arbitrary waveform output within ± 250 MHz of its local oscillator (LO) frequency. In this experiment, 4 LOs have been used to drive IQ mixers for different purposes, where an LO at 5.6 GHz (6 GHz) carrier frequency is used to control the qubits operating at about 5.5 GHz (5.9 GHz), and an LO at 6.55 GHz (6.5 GHz) carrier frequency is used for the dispersive readout of node A (node B) respectively.

The output of the readout microwave signal is first amplified by a traveling wave parametric amplifier (TWPA) [11] at the 10 mK stage (node B does not have a TWPA for qubit readout), then amplified by a cryogenic high electron mobility transistor (Low Noise Factory) at the 4 K stage. Two cryogenic circulators with low insertion loss are added between the TWPA and the cryogenic HEMT to block reflections and thermal noise emitted from the input of the cryogenic HEMT. An additional circulator is inserted between the TWPA drive line and the processor, to avoid any unexpected excitation of the qubits from the TWPA drive signal. The cryogenic HEMT output is further amplified by two room-temperature HEMT amplifiers (Miteq Corp.), then down-converted with an IQ mixer and captured by an ADC board.

The ADC board can perform on-board multi-channel demodulation of the captured waveform, yielding a single complex value $\widetilde{I}+i\widetilde{Q}$ in the phase space for each demodulation channel from a single measurement. This allows for the simultaneous readout of multiple qubits using frequency multiplexing [12]. With calibrated discrimination criteria in the $\widetilde{I}-\widetilde{Q}$ plane, a $|g\rangle$ or $|e\rangle$ state can be assigned to each $\widetilde{I}+i\widetilde{Q}$ value. Repeating this single-shot measurement several thousand times, we obtain the qubit state probabilities.

7

IV. DEVICE CHARACTERIZATION

A. Summary of device parameters

The parameters and typical performance of each qubit are summarized in Table S1. Note the linear inductance from the tunable coupler contributes to the total inductance of the qubit [13], reducing the maximum frequency of Q_2^n by a few hundred MHz. To counteract this effect, the size of Q_2^n's Josephson junctions was increased by 10% compared to that of the other qubits. The linear inductance from the coupler also weakens the nonlinearity of Q_2^n by about 70 MHz [13], which in turn affects the dispersive shift [14]. The readout duration for Q_2^n is correspondingly increased to compensate for this effect.

	$f_{eg}^{\max}$ (GHz)	f_{eg}^{idle} (GHz)	η (GHz)	T_1 (μs)	T_ϕ (μs)	f_{rr} (GHz)	τ_{rr} (ns)	F_g	F_e
Q_1^A	6.04	5.5050	-0.23	12	3.4	6.5032	250	0.982	0.944
Q_2^A	6.14	5.870	-0.15	7	3.8	6.5490	350	0.981	0.935
Q_3^A	6.03	5.4882	-0.23	7	3.8	6.6045	300	0.985	0.942
Q_1^B	6.08	5.4655	-0.23	29	4.2	6.5065	300	0.995	0.955
Q_2^B	6.25	5.8950	-0.16	11	4.4	6.5560	450	0.973	0.947
Q_3^B	6.16	5.4835	-0.23	20	2.9	6.6095	300	0.984	0.953

Table S1. Qubit parameters. Here $f_{eg}^{\max}$ is the qubit maximum frequency, f_{eg}^{idle} is the qubit idle frequency, η is the qubit nonlinearity, T_1 and T_ϕ are the qubit lifetime and pure dephasing time at the idle frequency respectively, f_{rr} is the readout resonator frequency, τ_{rr} is the readout length, F_g and F_e are the readout fidelity of the $|g\rangle$ and $|e\rangle$ states respectively.

To achieve a fast dispersive readout without introducing strong Purcell decay [15], we placed a Purcell filter between the readout resonators and the readout line. The Purcell filter is essentially a shorted half-wavelength coplanar waveguide resonator, similar to that used in Refs. 16–18. The filter has a resonant frequency of about 6.5 GHz, a weak coupling to the input port (coupling $Q_c \sim 2000$) and a strong coupling to the output port (coupling $Q_c \sim 25$). With this element, we are able to perform high-fidelity qubit readout in about 300 ns, even absent a TWPA or parametric amplifier [19]. The readout fidelity for the ground state $|g\rangle$ is ~ 0.98, primarily limited by the separation error and spurious excitations [20].

The readout fidelity of the excited state $|e\rangle$ is ~ 0.95, primarily limited by the lifetime of the qubit.

B. Single qubit gate characterization

We characterize the single qubit gate fidelities using Clifford-based randomized benchmarking (RB) [21–23]. A typical RB for Q_1^A is shown in Fig. S4. Table S2 summarizes the typical single qubit gate fidelities for all qubits in this experiment.
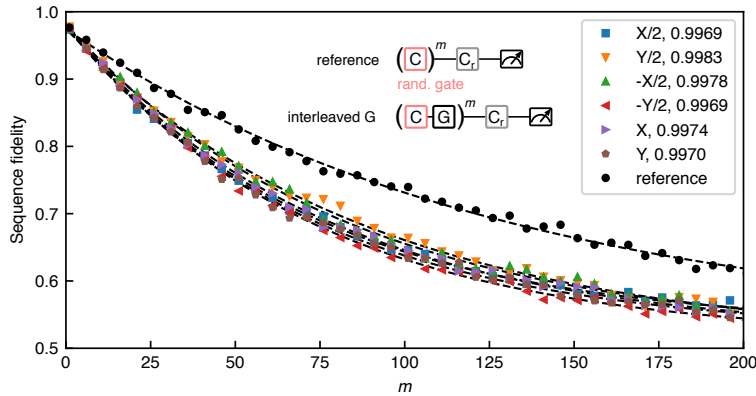

Figure S4. Single qubit randomized benchmarking for Q_1^A. Here C is a random Clifford gate and C_r is a Clifford gate that ideally restores the quantum state after the random gate sequence.

	X/2	-X/2	Y/2	-Y/2	X	Y	average
Q_1^A	0.9969	0.9978	0.9983	0.9969	0.9974	0.9970	0.9974
Q_2^A	0.9979	0.9969	0.9971	0.9980	0.9976	0.9973	0.9975
Q_3^A	0.9987	0.9985	0.9988	0.9970	0.9953	0.9983	0.9978
Q_1^B	0.9973	0.9990	0.9978	0.9976	0.9985	0.9981	0.9981
Q_2^B	0.9982	0.9951	0.9965	0.9959	0.9937	0.9969	0.9961
Q_3^B	0.9947	0.9968	0.9995	0.9967	0.9932	0.9983	0.9965

Table S2. Single qubit gate fidelities for all qubits in this experiment, as determined by randomized benchmarking.
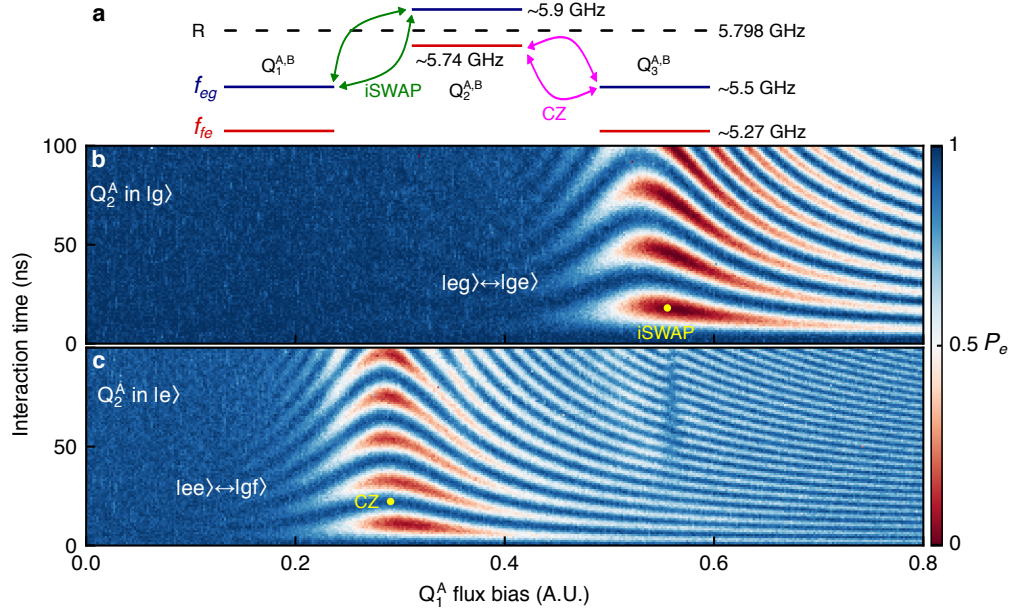
9

C. iSWAP and CZ gates

Figure S5. Implementation of two-qubit gates. **a,** Transition frequency diagram of the three qubits in each node, showing both the $g - e$ (f_{ge}) and $e - f$ (f_{ef}) transitions. The center qubits Q_2^n ($n = A, B$) are operated at ~ 5.9 GHz, and the side qubits $Q_{1,3}^n$ are operated at ~ 5.5 GHz. **b,** Vacuum Rabi oscillations for the two-qubit $|eg\rangle - |ge\rangle$ transition between Q_1^A and Q_2^A. An iSWAP gate can be implemented by enabling this oscillation for a duration of 15 ns, as marked by the yellow dot. **c,** Vacuum Rabi oscillations for the $|ee\rangle - |gf\rangle$ transition between Q_1^A and Q_2^A. A CZ gate can be implemented by enabling this oscillation for a duration of 21 ns, as marked by the yellow dot.

The transition frequency diagram of the three qubits in each node is shown in Fig. S5a. The central qubits Q_2^n ($n = A, B$) operate with their $g-e$ transition f_{eg} (blue) at ~ 5.9 GHz, while the other two qubits $Q_{1,3}^n$ operate at $f_{eg} \sim 5.5$ GHz (slightly detuned from one another). The $e - f$ transition f_{ef} (red) is around 5.9 GHz for Q_2^n and around 5.5 GHz for $Q_{1,3}^n$. With ~ 0.4 GHz detuning (~ 0.24 GHz detuning between the $|ee\rangle$-$|gf\rangle$ transition), the residual coupling between adjacent qubits is very small. During the quantum state transfer operation, Q_2^n is tuned to 5.798 GHz to resonantly interact with the communication mode R. At this frequency, the detuning between Q_2^n and the side qubits $Q_{1,3}^n$ is not small enough to avoid unwanted stray coupling, so we apply detuning pulses to $Q_{1,3}^n$ to reduce their transition

10

frequencies by about 200 MHz during this process.

To swap a quantum state from $Q_{1,3}^n$ to Q_2^n (initially in the $|g\rangle$ state), we bias $Q_{1,3}^n$ so its $g - e$ transition is resonant with that of Q_2^n, initiating vacuum Rabi oscillation between the $|eg\rangle$ and $|ge\rangle$ states, as shown in Fig. S5b. At $\tau_{\text{swap}} = \pi/2g_{j,2}^n = 15$ ns, we complete the $|eg\rangle \to -i|ge\rangle$ iSWAP process. Ideally, the $|ee\rangle$ state is unchanged under this gate, but as shown in Fig. S5c, due to the weak nonlinearity of Q_2^n, if both qubits are in the $|e\rangle$ state, stray coupling between the $|gf\rangle$ state and the $|ee\rangle$ state can cause state leakage during the iSWAP gate. Fortunately, in this experiment, the receiver qubit is ideally always in its $|g\rangle$ state when we transfer states using the iSWAP gate, so this state leakage is not a concern.
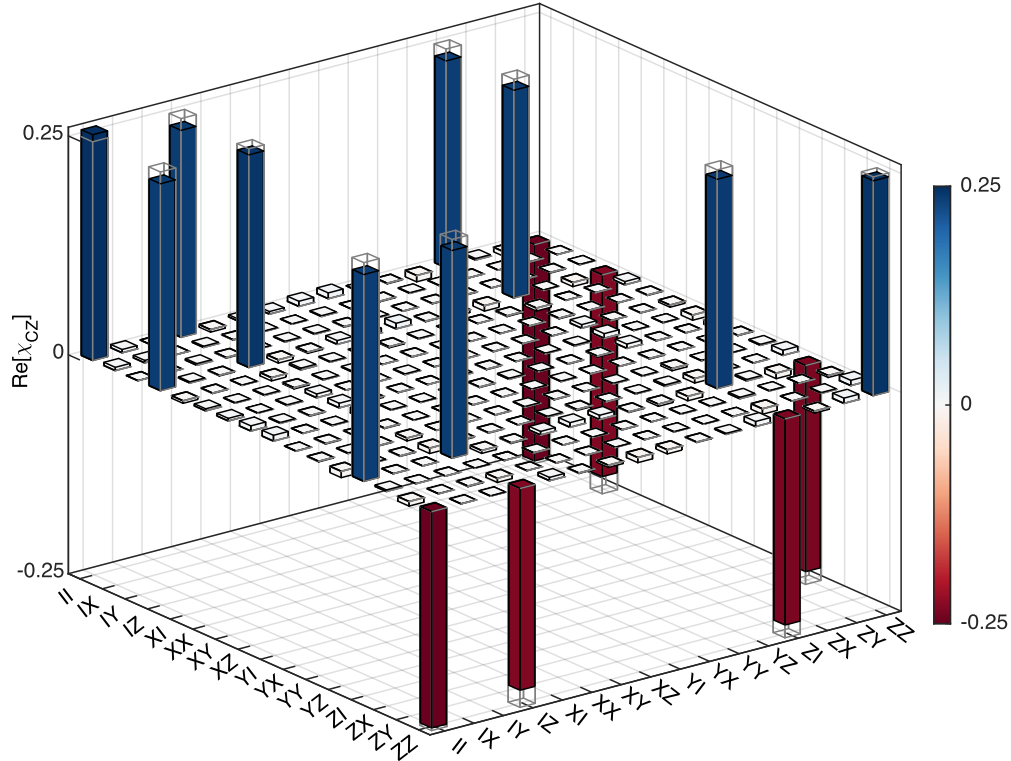

Figure S6. Quantum process tomography of the CZ gate between Q_1^A and Q_2^A. The solid color and gray outline bars are for the measured and ideal values respectively. The CZ gate has a process fidelity of 0.958 ± 0.007.

To characterize the transfer efficiency of the iSWAP gate, we compare the Q_2^n $|e\rangle$ final state probability P_e from two experiments: In one experiment, we apply a π pulse to Q_2^n directly, and then measure; in the other experiment, we apply a π pulse to $Q_{1,3}^n$ and then transfer the excitation to Q_2^n using an iSWAP gate, followed by measurement. These two

experiments are carried out back-to-back and repeated 1000 times. We compare the average $\langle P_e \rangle$ from the two experiments, and find that the iSWAP gate has a transfer efficiency $\eta_{\text{iSWAP}} \approx 0.99$.

	$Q_1^A - Q_2^A$	$Q_3^A - Q_2^A$	$Q_1^B - Q_2^B$	$Q_3^B - Q_2^B$	average
$\mathcal{F}_{CZ}$	0.958(7)	0.945(8)	0.952(5)	0.944(7)	0.950(6)

Table S3.   CZ gate fidelities, determined by process tomography.

The CZ gate here is implemented utilizing the $|f\rangle$ state of Q_2^n, as proposed in Ref. 24 and demonstrated in Refs. 25 and 26. When biasing $Q_{1,3}^n$ to be resonant with the $|e\rangle$-$|f\rangle$ transition frequency of Q_2^n, a vacuum Rabi oscillation between the $|ee\rangle$ and $|gf\rangle$ state can be observed, as shown in Fig. S5c. If the interaction is turned on for $\tau_{\text{CZ}} = \pi/\sqrt{2}g_{j,2}^n \approx 21$ ns, $j = 1, 3$, the quantum state completes an $|ee\rangle \rightarrow -i|gf\rangle \rightarrow -|ee\rangle$ round trip and acquires a π phase relative to the other states, as required for this gate [24].

We perform quantum process tomography to characterize the CZ gate between Q_1^A and Q_2^A here, yielding the process matrix χ_{CZ} shown in Fig. S6, with a process fidelity of $\mathcal{F}_{CZ} = \text{Tr}(\chi_{CZ} \cdot \chi_{CZ,\text{ideal}}) = 0.958 \pm 0.007$, here $\chi_{CZ,\text{ideal}}$ is the process matrix for the ideal CZ gate, and the error bar is the standard deviation of repeated measurements. The fidelities of all the CZ gates are summarized in Table S3, with an average fidelity of 0.950 ± 0.006, here the error bar is the standard deviation of the four CZ gate fidelities.
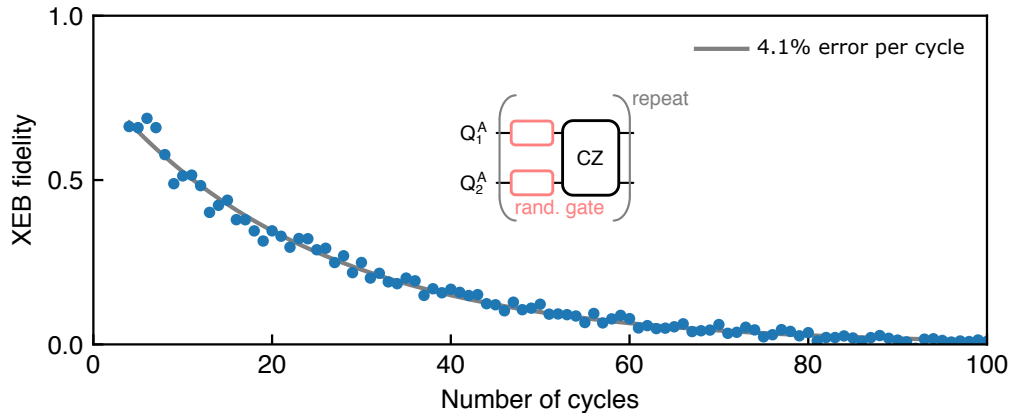

Figure S7. Cross-entropy benchmarking of the CZ gate, with an error of 4.1% per cycle.

In addition to quantum process tomography, we use the cross-entropy benchmarking

(XEB) technique [27] to estimate the fidelity of the CZ gate, where we measure an error of 4.1% per cycle. Subtracting the single-qubit gate errors, the CZ gate fidelity is 0.964, in good agreement with the process tomography fidelity. Note that CZ gate fidelities > 0.99 can be achieved with an optimized adiabatic gate [23, 28] or tunable coupling [13, 27, 29].

A dynamic phase is accumulated by each qubit when performing the two-qubit gates, due to the change of the qubit frequency during the interaction. This dynamic phase can be physically corrected by applying a calibrated Z rotation. Alternatively, to simplify the control sequence, here we adjust the phase of the tomography pulses to correct for the dynamic phase shift when performing quantum state tomography. Similarly, we adjust the phase of the second $Y/2$ gate on the target qubit to correct for the dynamic phase shift when performing a CNOT gate.
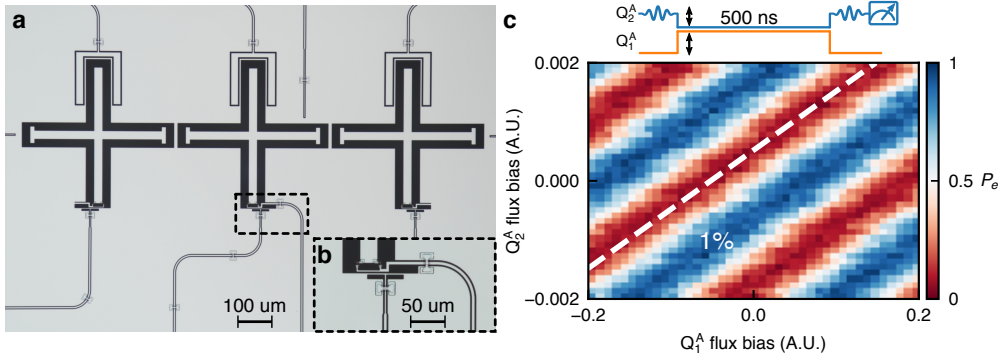
D. Flux crosstalk

Figure S8. Measurement of qubit and coupler magnetic flux crosstalk. **a,** Xmon qubit design adopted from Ref. 30, with a gradiometer flux control line design. **b,** Magnified view of the flux control line design. **c,** Characterization of the flux crosstalk between Q_1^A and Q_2^A, using Ramsey interference. The control pulse sequence is shown on top, where the black double-headed arrows represent the effect of the control fluxes varied in the measurement. The white dashed line is a representative contour line of the data, along which the fluxes from the control lines for Q_1^A and Q_2^A cancel one another. The slope of this line, which is 1% here, represents the flux crosstalk between these two qubits.

There are 6 qubits and 2 tunable couplers in the quantum network measured here, each of which has an independent flux control line. It is very important to mitigate the flux

crosstalk between these channels, to achieve the highest fidelity qubit control and state transfer. First, we implemented a gradiometer design for the flux control line of each qubit, in order to minimize the flux crosstalk, as shown in Fig. S8a and b. We then measured the flux crosstalk between qubit pairs using Ramsey interference. We find that the crosstalk between neighbouring qubits is about 1%, where a representative measurement in shown in Fig. S8c. The flux crosstalk between the cable-coupled qubits Q_2^n and their adjustable couplers G^n in each node is estimated to be 3-6%, using spectroscopy measurements (not shown).

V.   QUBIT-CABLE COUPLING

The $\ell_{cb} = 1$ m long NbTi cable has a specific capacitance $\mathscr{C}_{cb} = 96.2$ pF/m and a specific inductance $\mathscr{L}_{cb} = 240.5$ nH/m (as provided by the cable manufacturer). The cable is galvanically connected to the tunable couplers by a short segment of CPW line of length $\ell_c \approx 2$ mm patterned on each quantum processor die. The CPW line has a specific capacitance $\mathscr{C}_{cpw} = 173$ pF/m and specific inductance $\mathscr{L}_{cpw} = 402$ nH/m. The mth standing mode in the CPW-cable-CPW channel can be modeled as a lumped element series LC resonator [7], with parameters given by

$$L_m \approx \frac{1}{2}(\mathscr{L}_{cp}\ell_{cp} + 2\mathscr{L}_{cpw}\ell_c) = 121 \text{ nH}, \tag{S3}$$

$$\omega_m \approx m\omega_{\text{FSR}}, \tag{S4}$$

$$C_m = \frac{1}{\omega_m^2 L_m}. \tag{S5}$$

Each qubit Q_2^n ($n = A, B$) is coupled to the channel via a tunable coupler G^n with the same design as in Ref. 1. This configuration is accurately modeled [13, 31] as a tunable inductance given by

$$M_c^n = \frac{L_g^2}{2L_g + L_w + L_T^n/\cos\delta^n}, \tag{S6}$$

where δ^n is the phase across the coupler Josephson junction, L_T^n is the coupler junction inductance at $\delta^n = 0$, $L_g = 0.2$ nH, and $L_w \approx 0.1$ nH represents the stray wiring inductance, which cannot be ignored when L_T^n becomes very small [1].

In the harmonic limit and assuming weak coupling, the coupling between qubit Q_2^n and

the mth mode is [13, 31]

$$g_m^n = -\frac{M_c^n}{2} \sqrt{\frac{\omega_m \omega_2^n}{(L_g + L_q^n)(L_g + L_m)}}, \tag{S7}$$

where $L_q^n \approx 8.4$ nH is the qubit Q_2^n inductance and $\omega_2^n/2\pi$ is $Q_2^{n\text{'s}}$ operating frequency. We see that $g_m^n \propto \sqrt{\omega_m} \propto \sqrt{m}$, a well-known result for multi-mode coupling [32]. It is experimentally more practical to approximate the coupling by a single value g^n, because as the mode number $m \sim 55 \gg 1$ near 5.8 GHz, the variation in g_m^n with m within the frequency range of interest is small.
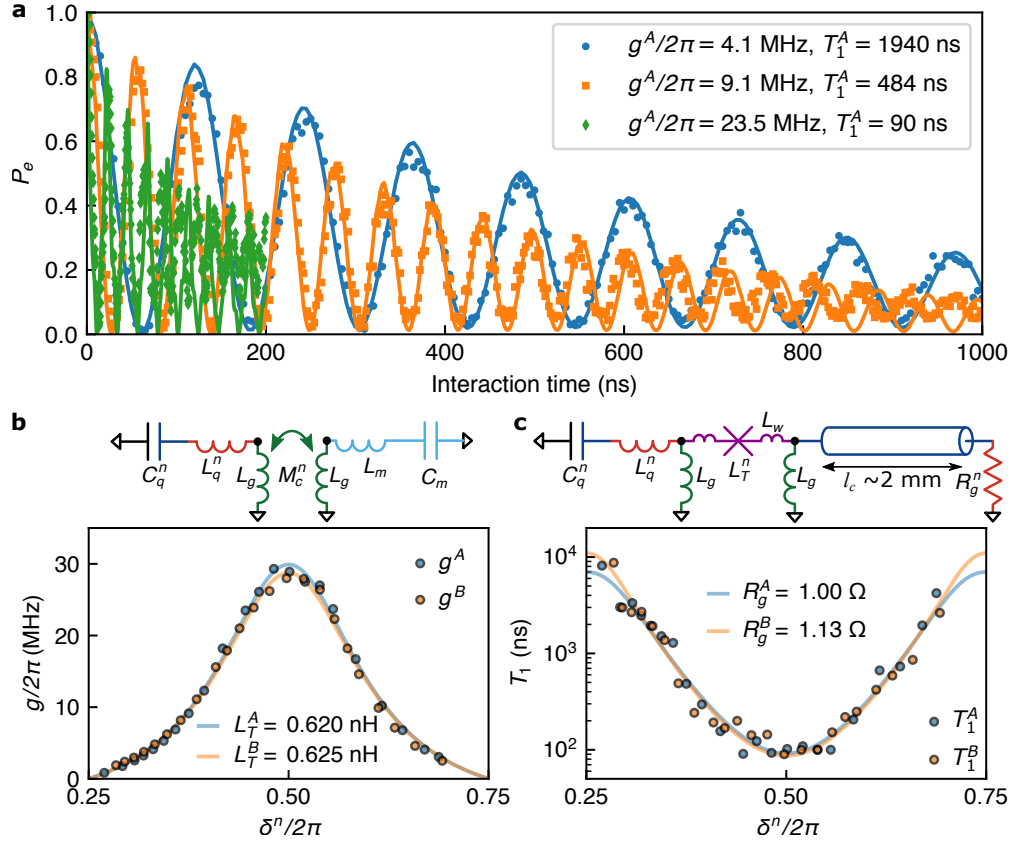

Figure S9.   Tunable coupler characterization. **a,** Vacuum Rabi oscillations between qubit Q_2^A and the communication mode R at different coupling strength $g^A/2\pi$. Fitting the data gives $g^A/2\pi$ and the qubit lifetime T_1^A during the interaction. **b,** $g^n/2\pi$ versus δ^n. Top: lumped-element linear circuit model for the inductive coupling between the qubit Q_2^n and the communication mode R, which is modeled as a series LC resonator. **c,** Q_2^n lifetime T_1^n versus δ^n during the interaction. Top: phenomenological circuit model for calculating the qubit loss, assuming a loss channel R_g^n shunting the wirebond connection to ground.

To characterize the tunable couplers, we vary the coupler junction phase δ^n and tune the qubit Q_2^n to resonantly interact with the communication mode R, as shown in Fig. S9a. The coupling strength $g^n/2\pi$ versus δ^n is shown in Fig. S9b, which is obtained by fitting a series of vacuum Rabi oscillations similar to Fig. S9a (for details of the fitting, see Section VI). We fit the analytical model, Eq. (S7), to the data in Fig. S9b, and find that $L_T^A = 0.620$ nH and $L_T^B = 0.625$ nH. Maximum coupling occurs at the junction phase $\delta^n = \pi$, where $g_{\max}^A/2\pi \approx$ 29 MHz and $g_{\max}^B/2\pi \approx 28$ MHz. The coupling can be turned off by setting $\delta^n = \pi/2$, making $L_T^n/\cos\delta^n$ very large.

It can be seen from Fig. S9a that the envelope of the vacuum Rabi oscillation decays faster as the coupling strength increases. This is attributed to the lossy wirebond interface, which not only introduces dissipation to the communication channel, but also affects the qubit coherence. Here we use a phenomenological model, shown at the top of Fig. S9c, to characterize the qubit loss at different coupling strengths, where we simply assume a lumped resistor R_g^n shunting the wirebond interface to ground. We fit the model with the measured qubit T_1^n (log scale), and find that the model agrees very well with the data, with $R_g^A = 1.00$ Ω and $R_g^B = 1.13$ Ω.

VI. NUMERICAL SIMULATIONS

The full quantum system can be modeled with the following rotating-frame, multi-qubit, multi-mode communication channel Hamiltonian:

$$H/\hbar = \sum_{\substack{n=A,B \\ i=1,2,3}} \Delta\omega_i^n \sigma_i^{n\dagger}\sigma_i^n + \sum_{m=1}^{M}\left(m - \frac{M+1}{2}\right)\omega_{\mathrm{FSR}}a_m^\dagger a_m \tag{S8}$$
$$+ \sum_{\substack{n=A,B \\ j=1,3}} g_{j,2}^n\left(\sigma_2^n\sigma_j^{n\dagger} + \sigma_2^{n\dagger}\sigma_j^n\right)$$
$$+ \sum_{m=1}^{M} g^A\left(\sigma_2^A a_m^\dagger + \sigma_2^{A\dagger}a_m\right) + \sum_{m=1}^{M}(-1)^m g^B\left(\sigma_2^B a_m^\dagger + \sigma_2^{B\dagger}a_m\right),$$

where σ_i^n and a_m are the annihilation operators for qubit Q_i^n and the mth standing-wave mode respectively, $\Delta\omega_i^n$ is the qubit frequency detuning with respect to the rotating frame frequency, and M is the number of standing modes included in the simulation (always chosen to be an odd number). The rotating frame frequency is set at the center of the standing-mode frequencies, i.e. for mode number $m = (M+1)/2$. Note the sign of g^B alternates

16

with the mode number m due to the parity dependence of the standing wave mode [33, 34]. In this experiment, not all components are involved simultaneously, and in certain cases the full Hamiltonian can be simplified.

In Fig. 2b in the main text, where only Q_2^A and the standing modes are interacting, the Hamiltonian can be simplified to

$$H/\hbar = \sum_{m=1}^{M} \left(m - \frac{M+1}{2}\right) \omega_{\text{FSR}} a_m^\dagger a_m + \sum_{m=1}^{M} g^A \left(\sigma_2^A a_m^\dagger + \sigma_2^{A\dagger} a_m\right), \tag{S9}$$

where we choose $M = 5$ standing modes, with the third mode $m = 3$ the communication mode R, and Q_2^A is assumed to be on resonant with R such that $\Delta\omega_2^A = 0$. Decoherence is taken into account using the Lindblad master equation. The quantum state evolution is calculated using QuTiP [35]. The five standing modes included in the model here have measured lifetimes of 256 ns, 177 ns, 473 ns, 200 ns, and 370 ns respectively. We first compare the numerical simulations using the qubit intrinsic lifetime $T_1 = 7$ us, and find discrepancies with the data (see the grey line in Fig. 2b of the main text). As discussed in Section II, the loss in the channel is dominated by the wirebond interface. Changing the coupler inductance does not change the participation of the lossy wirebond interface in the channel, so the lifetime of the standing modes should not be affected by the coupling strength. On the other hand, when the coupling is turned on, the qubit is exposed to the lossy wirebond interface, introducing a new loss channel to the qubit coherence. This unwanted side-effect is characterized by the phenomenological circuit model shown in Section V. We fit the master equation simulation to the experimental data and find that the qubit T_1 is decreased to 1.4 μs during the interaction (red line in Fig. 2b in the main text). Similarly, we fit a series of vacuum Rabi oscillations, as shown in Fig. S9a, to obtain the coupling strength $g^n/2\pi$ (Fig. S9b) and the qubit lifetime T_1^n (Fig. S9c) at different coupler junction phases δ^n.

In Fig. 2c in the main text, where the side qubits $Q_{1,3}^n$ are tuned far in frequency from Q_2^n, the state transfer process can be modeled with the simplified Hamiltonian:

$$H/\hbar = \sum_{n=A,B} \Delta\omega_2^n \sigma_2^{n\dagger} \sigma_2^n + \sum_{m=1}^{M} \left(m - \frac{M+1}{2}\right) \omega_{\text{FSR}} a_m^\dagger a_m \tag{S10}$$

$$+ \sum_{m=1}^{M} g^A \left(\sigma_2^A a_m^\dagger + \sigma_2^{A\dagger} a_m\right) + \sum_{m=1}^{M} (-1)^m g^B \left(\sigma_2^B a_m^\dagger + \sigma_2^{B\dagger} a_m\right),$$

17

where we include $M = 5$ standing modes in the simulations, and R is the third mode, $m = 3$. Ideally, for the hybrid state transfer scheme [36], both qubits Q_2^n should be resonant with R, such that $\Delta\omega_2^n = 0$, and the coupling g^A and g^B should be set to the same coupling strength g_0 simultaneously for a duration τ. In the experiment, we vary the qubit frequencies as well as the relative amplitude and delay between g_A and g_B, to optimize the transfer fidelity. It is found that a higher fidelity is achieved with a delay of $\Delta\tau = 13$ ns between the initial turn-on for g_A and g_B (in other words, both g_A and g_B are turned on for a duration of τ, but g^B is turned on 13 ns later than g^A). With this experimentally-optimized $\Delta\tau$, we fit the model to the data shown in Fig. 2c in the main text, and find that $\Delta\omega_2^A/2\pi = -0.95$ MHz, $\Delta\omega_2^B/2\pi = -1.79$ MHz, $g_A/2\pi = 4.08$ MHz and $g_B/2\pi = 4.06$ MHz (these are the parameters for the grey line in Fig. 2c in the main text).

In Fig. 3b of the main text, the numerical ρ^A is calculated using the CZ gate process matrix χ_{CZ} measured in Section IV C, assuming the single-qubit rotation gates are ideal (using their measured fidelities has almost no impact on the results). The numerical GHZ state fidelity is 0.938, agreeing well with the experiment. The prepared GHZ state fidelity is primarily limited by the CZ gate fidelity, which could be improved by using an optimized adiabatic gate [23, 28] or using tunable coupling [13, 27, 29]. Some one-step GHZ state preparation methods utilizing a common bus resonator may also be able to prepare high-fidelity GHZ states [37, 38]. In Fig. 3c of the main text, the numerical ρ^B is calculated by applying the state transfer process $\chi^{\otimes 3}$ and the decoherence process to ρ^A from Fig. 3b. The fidelity of ρ^B is primarily limited by the state transfer fidelity $\mathcal{F}^p$, which might be improved by optimizing the coupler circuit design or using a coaxial cable made with different superconducting material, e.g. aluminium, as discussed in Section II.

In Fig. 4b in the main text, the control pulse for "ST/2" is similar to that for "ST" as shown in Fig. 2c inset, except the coupling strength g^A and g^B, the interaction time τ and the delay $\Delta\tau$, are experimentally tuned to optimize the Bell state fidelity. With $\Delta\tau = 5$ ns, as determined experimentally, we fit the data in Fig. S10, which is similar to Fig.2c in the main text, and obtain $\Delta\omega_2^A/2\pi = 4.7$ MHz, $\Delta\omega_2^B/2\pi = 5.4$ MHz, $g_A/2\pi = 2.89$ MHz and $g_B/2\pi = 6.11$ MHz. The numerical Bell state fidelity is 0.915, agreeing well with the experiment. This Bell state fidelity is primarily limited by the channel loss.
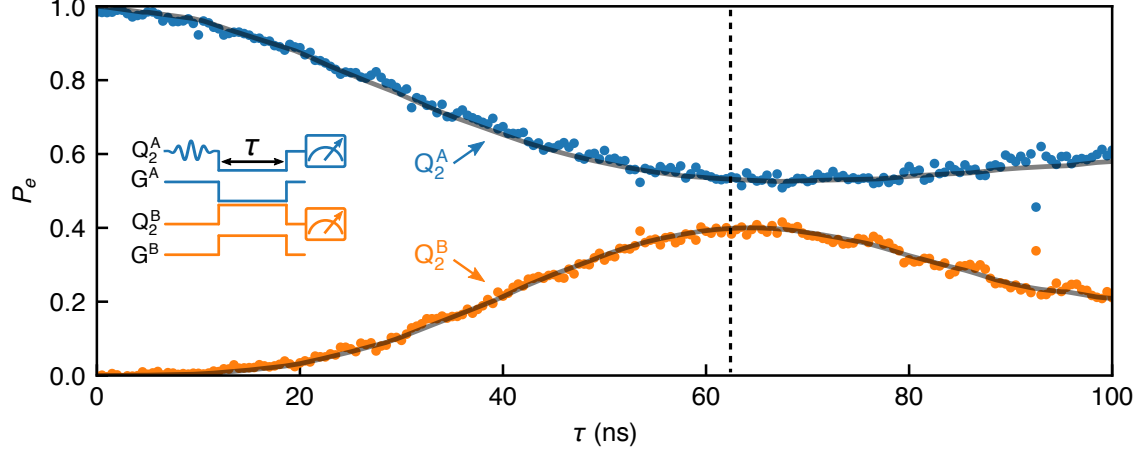
Figure S10. The "ST/2" process, where half a photon is sent from node A to node B. The control pulse sequence here is similar to that in Fig. 2c in the main text, except the coupling strength g^A and g^B, the interaction time τ and the delay $\Delta\tau$, are experimentally tuned to optimize the Bell state fidelity. The dashed line marks the point where the Bell state fidelity is optimal.

In Fig. 4c, we calculate the theoretical ρ_{II} by applying χ_{CZ} (measured in Section IV C) to ρ_I from Fig. 4b, assuming the single qubit rotation gates are ideal.

In Fig. 4d, we calculate the theoretical ρ_{III} by applying χ_{CZ} and decoherence process to ρ_{II} from Fig. 4c, again assuming the single-qubit rotation gates are ideal. The decoherence process is applied to Q_1^n to account for the idling of 70 ns during the application of CNOT gates to Q_3^n. The fidelity of ρ_{II} and ρ_{III} is primarily limited by the fidelity of ρ_I and the CZ gates.

[1] Zhong, Y. P. *et al.* Violating Bell's inequality with remotely connected superconducting qubits. *Nature Physics* **15**, 741–744 (2019).

[2] Kelly, J. S. *Fault-tolerant superconducting qubits.* Ph.D. thesis, University of California Santa Barbara (2015).

[3] Dunsworth, A. *et al.* A method for building low loss multi-layer wiring for superconducting microwave devices. *Applied Physics Letters* **112**, 063502 (2018).

[4] Dolan, G. J. Offset masks for lift-off photoprocessing. *Applied Physics Letters* **31**, 337–339 (1977).

[5] Dunsworth, A. *et al.* Characterization and reduction of capacitive loss induced by sub-micron Josephson junction fabrication in superconducting qubits. *Applied Physics Letters* **111**, 022601 (2017).

[6] Megrant, A. *et al.* Planar superconducting resonators with internal quality factors above one million. *Applied Physics Letters* **100**, 113510 (2012).

[7] Pozar, D. M. *Microwave engineering* (Wiley, 2011), fourth edn.

[8] Kurpiers, P., Walter, T., Magnard, P., Salathe, Y. & Wallraff, A. Characterizing the attenuation of coaxial and rectangular microwave-frequency waveguides at cryogenic temperatures. *EPJ Quantum Technology* **4**, 1–15 (2017).

[9] Burkhart, L. D. *et al.* Error-detected state transfer and entanglement in a superconducting quantum network. *arXiv preprint arXiv:2004.06168* (2020).

[10] Yan, F. *et al.* Tunable coupling scheme for implementing high-fidelity two-qubit gates. *Physical Review Applied* **10**, 054062 (2018).

[11] Macklin, C. *et al.* A near-quantum-limited Josephson traveling-wave parametric amplifier. *Science* **350**, 307–310 (2015).

[12] Chen, Y. *et al.* Multiplexed dispersive readout of superconducting phase qubits. *Applied Physics Letters* **101**, 182601 (2012).

[13] Chen, Y. *et al.* Qubit architecture with high coherence and fast tunable coupling. *Physical Review Letters* **113**, 220502 (2014).

[14] Koch, J. *et al.* Charge-insensitive qubit design derived from the Cooper pair box. *Physical Review A* **76**, 042319 (2007).

[15] Houck, A. *et al.* Controlling the spontaneous emission of a superconducting transmon qubit. *Physical Review Letters* **101**, 080502 (2008).

[16] Satzinger, K. J. *et al.* Quantum control of surface acoustic-wave phonons. *Nature* **563**, 661–665 (2018).

[17] Bienfait, A. *et al.* Phonon-mediated quantum state transfer and remote qubit entanglement. *Science* **364**, 368–371 (2019).

[18] Jeffrey, E. *et al.* Fast accurate state measurement with superconducting qubits. *Physical Review Letters* **112**, 190504 (2014).

[19] Vijay, R., Slichter, D. & Siddiqi, I. Observation of quantum jumps in a superconducting artificial atom. *Physical Review Letters* **106**, 110502 (2011).

[20] Walter, T. *et al.* Rapid high-fidelity single-shot dispersive readout of superconducting qubits. *Physical Review Applied* **7**, 054020 (2017).

[21] Ryan, C., Laforest, M. & Laflamme, R. Randomized benchmarking of single-and multi-qubit control in liquid-state NMR quantum information processing. *New Journal of Physics* **11**, 013034 (2009).

[22] Brown, K. R. *et al.* Single-qubit-gate error below $\mathbf{10^{-4}}$ in a trapped ion. *Physical Review A* **84**, 030303 (2011).

[23] Barends, R. *et al.* Superconducting quantum circuits at the surface code threshold for fault tolerance. *Nature* **508**, 500–503 (2014).

[24] Strauch, F. W. *et al.* Quantum logic gates for coupled superconducting phase qubits. *Physical Review Letters* **91**, 167005 (2003).

[25] DiCarlo, L. *et al.* Preparation and measurement of three-qubit entanglement in a superconducting circuit. *Nature* **467**, 574–578 (2010).

[26] Yamamoto, T. *et al.* Quantum process tomography of two-qubit controlled-Z and controlled-NOT gates using superconducting phase qubits. *Physical Review B* **82**, 184515 (2010).

[27] Arute, F. *et al.* Quantum supremacy using a programmable superconducting processor. *Nature* **574**, 505–510 (2019).

[28] Martinis, J. M. & Geller, M. R. Fast adiabatic qubit gates using only σ_z control. *Physical Review A* **90**, 022307 (2014).

[29] Xu, Y. *et al.* High-fidelity, high-scalability two-qubit gate scheme for superconducting qubits. *arXiv preprint arXiv:2006.11860* (2020).

[30] Barends, R. *et al.* Coherent Josephson qubit suitable for scalable quantum integrated circuits. *Physical Review Letters* **111**, 080502 (2013).

[31] Geller, M. R. *et al.* Tunable coupler for superconducting Xmon qubits: Perturbative nonlinear model. *Physical Review A* **92**, 012320 (2015).

[32] Sundaresan, N. M. *et al.* Beyond strong coupling in a multimode cavity. *Physical Review X* **5**, 021035 (2015).

[33] Pellizzari, T. Quantum networking with optical fibres. *Physical Review Letters* **79**, 5242 (1997).

[34] Vogell, B., Vermersch, B., Northup, T., Lanyon, B. & Muschik, C. Deterministic quantum state transfer between remote qubits in cavities. *Quantum Science and Technology* **2**, 045003 (2017).

[35] Johansson, J., Nation, P. & Nori, F. QuTiP: An open-source Python framework for the dynamics of open quantum systems. *Computer Physics Communications* **183**, 1760–1772 (2012).

[36] Wang, Y.-D. & Clerk, A. A. Using dark modes for high-fidelity optomechanical quantum state transfer. *New Journal of Physics* **14**, 105010 (2012).

[37] Zheng, S.-B. One-step synthesis of multiatom Greenberger-Horne-Zeilinger states. *Physical Review Letters* **87**, 230404 (2001).

[38] Song, C. *et al.* 10-qubit entanglement and parallel logic operations with a superconducting circuit. *Physical Review Letters* **119**, 180511 (2017).